



P-doped $\text{Co}_3\text{S}_4/\text{NiS}_2$ heterostructures embedded in N-doped carbon nanoboxes: Synergistical electronic structure regulation for overall water splitting

Shoushuang Huang^a, Shuzhen Ma^a, Libin Liu^a, Zhiqiang Jin^a, Pengyan Gao^a, Kaimei Peng^{b,*}, Yong Jiang^a, Amene Naseri^{c,*}, Zhangjun Hu^{d,*}, Jiuju Zhang^e

^a School of Environmental and Chemical Engineering, Shanghai University, Shanghai 200444, China

^b School of Chemistry and Chemical Engineering, Qiannan Normal University for Nationalities, Duyun 558000, China

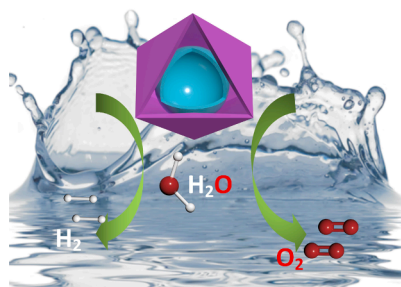
^c Nanotechnology Department, Agricultural Biotechnology Research Institute of Iran (ABRII), Agricultural Research, Education, and Extension Organization (AREEO), Karaj 3135933151, Iran

^d Division of Molecular Surface Physics & Nanoscience, Department of Physics, Chemistry and Biology, Linköping University, Linköping 58183, Sweden

^e Institute for Sustainable Energy/College of Sciences, Shanghai University, Shanghai 200444, China

GRAPHICAL ABSTRACT

P-doped $\text{Co}_3\text{S}_4/\text{NiS}_2$ heterostructures embedded in N-doped carbon nanoboxes were rationally synthesized via a pyrolysis-sulfidation-phosphorization strategy, which exhibited excellent electrocatalytic activity for alkaline water splitting.



ARTICLE INFO

Keywords:

Prussian blue analogues
Sulfides
Heteroatom doping
Electrocatalysis
Heterojunctions

ABSTRACT

Water splitting using transition metal sulfides as electrocatalysts has gained considerable attention in the field of renewable energy. However, their electrocatalytic activity is often hindered by unfavorable free energies of adsorbed hydrogen and oxygen-containing intermediates. Herein, phosphorus (P)-doped $\text{Co}_3\text{S}_4/\text{NiS}_2$ heterostructures embedded in N-doped carbon nanoboxes were rationally synthesized via a pyrolysis-sulfidation-phosphorization strategy. The hollow structure of the carbon matrix and the nanoparticles contained within it not only result in a high specific surface area, but also protects them from corrosion and acts as a conductive pathway for efficient electron transfer. Density functional theory (DFT) calculations indicate that the introduction of P dopants improves the conductivity of NiS_2 and Co_3S_4 , promotes the charge transfer process, and creates new electrocatalytic sites. Additionally, the $\text{NiS}_2\text{-Co}_3\text{S}_4$ heterojunctions can enhance the adsorption

* Corresponding authors.

E-mail addresses: pkmchem@sgmtu.edu.cn (K. Peng), a.naseri@abrii.ac.ir (A. Naseri), zhangjun.hu@liu.se (Z. Hu).

<https://doi.org/10.1016/j.jcis.2023.08.092>

Received 1 May 2023; Received in revised form 9 August 2023; Accepted 13 August 2023

Available online 14 August 2023

0021-9797/© 2023 The Authors. Published by Elsevier Inc. This is an open access article under the CC BY license (<http://creativecommons.org/licenses/by/4.0/>).

efficiency of hydrogen intermediates (H^*) and lower the energy barrier of water splitting via a synergistic effect with P-doping. These characteristics collectively enable the titled catalyst to exhibit excellent electrocatalytic activity for water splitting in alkaline medium, requiring only small overpotentials of 150 and 257 mV to achieve a current density of 10 mA cm^{-2} for hydrogen and oxygen evolution reactions, respectively. This work sheds light on the design and optimization of efficient electrocatalysts for water splitting, with potential implications for renewable energy production.

1. Introduction

The pressing issues of environmental pollution and the energy crisis have led to a growing demand for renewable and clean energy sources and associated conversion systems. Among these systems, electrochemical water splitting has gained significant attention as a potential means of producing green and pure hydrogen energy [1,2]. Nevertheless, the development of more efficient and stable catalysts represents a significant challenge in the advancement of these technologies and devices. To improve the energy conversion efficiency of electrocatalytic water splitting, the use of low-cost, efficient, and stable earth-abundant electrocatalysts is crucial in addressing the high overpotential and slow reaction kinetics of the hydrogen evolution reaction (HER) and oxygen evolution reaction (OER) [3]. Noble metal catalysts such as ruthenium, platinum, iridium, and their oxides have exceptional catalytic activity and stability, but their practical application is limited due to paucity of earth resources and expensive pricing.

Transition metal complexes, including oxides [4], sulfides [5,6], selenides [7,8], phosphides [9,10], carbides [11,12], and nitrides [13], have been investigated as substitutes for precious metal catalysts due to their abundance and unique chemical properties. Among them, nickel and cobalt-based sulfides, with tunable stoichiometric ratios and distinctive crystal structures, have demonstrated good performance in both the HER and OER [14–16]. However, the Gibbs free energy of hydrogen adsorption (ΔG_{H^*}) on the surface of these sulfides is often more positive than the optimal value of approximately 0 eV, hindering the adsorption of the hydrogen intermediate (H^*) [17–19]. Particularly, the effective adsorption of H^* is a critical prerequisite for HER, ultimately determining the electrocatalytic reaction rate [20]. In this regard, the electrocatalytic activity of nickel and cobalt-based sulfides for HER is largely dependent on balancing the adsorption of H^* with the removal of H_2 from their surface. Therefore, the optimization of the electronic structure of nickel (cobalt) sulfide-based electrocatalysts is a promising strategy to improve their performance.

Recently, the construction of heterostructures represents a promising approach for improving the electrocatalytic activity of catalysts in various electrochemical reactions. The heterostructure interfaces can provide additional active sites for electrocatalytic reactions, and the synergistic effect between different components can enhance the electron transfer rate and facilitate the adsorption/desorption of reactants and intermediates [21]. In addition, the electronic properties and crystal structures of different components can be tailored to achieve optimized electrocatalytic performance [22–24]. For instance, Xia et al. [25] reported that the hollow CoP@MoS_2 hetero-frames displayed excellent electrochemical catalytic performance in acidic solution due to the strong interaction between CoP and MoS_2 . Zhai et al. [26] found that the $\text{NiMoO}_x/\text{NiMoS}$ heterostructure array exhibited ultra-small overpotentials of 186 mV for OER and 38 mV for HER at 10 mA cm^{-2} , respectively. Therefore, the construction of nickel/cobalt-based sulfides heterostructures holds great potential for the design and development of efficient electrocatalysts for HER and OER.

Besides construction of heterojunctions, atomic doping is another effective way for improving the performance of catalysts by enhancing their electronic structure, balancing the hydrogen Gibbs free energy, and boosting their electrical conductivity [27–29]. This is because the doping of heteroatoms can modify the interaction of intermediates at the active site and alter the electron density close to the d-band orbital. For

example, Wang et al. [30] designed and synthesized vanadium-doped Ni_3S_2 nanorod arrays ($\text{V-Ni}_3\text{S}_2/\text{NF}$) grown on NF, which exhibited a low overpotential of only 189 mV to drive 100 mA cm^{-2} . Chong et al. [31] synthesized hierarchical phosphorus-oxygen incorporated cobalt sulfide spherical micro/nano-reactor by one-step liquid phase sulphuration and subsequent vapor phase phosphorization method, resulting in enhanced electrocatalytic behavior toward overall water splitting performance due to the dual-heteroatoms incorporation. Especially, phosphorus doping has been widely used to modify the electrical structure of catalysts and has shown effective application in electrocatalytic reactions. However, the use of phosphorus-doped sulfides in HER and OER has received relatively few reports, indicating the need for further research and exploration to control the catalytic performance of sulfides through precise adjustment of their structure and phosphorus doping.

Herein, we present a distinctive three-step approach, namely pyrolysis-sulfidation-phosphorization, to fabricate P-doped $\text{NiS}_2/\text{Co}_3\text{S}_4$ hetero-nanoparticles embedded in N-doped carbon (NC) nanoboxes, as a bifunctional electrocatalyst for HER and OER in alkaline solution. The resulting P-doped $\text{NiS}_2/\text{Co}_3\text{S}_4$ nanoboxes consist of an external nanoshell of N-doped carbon and an internal core of P-doped $\text{NiS}_2/\text{Co}_3\text{S}_4$ hetero-nanoparticles, which provides a large inner surface area, thus increasing the number of active sites and accelerating electrolyte diffusion and transmission. DFT calculations indicate that the P-doping and the formed $\text{NiS}_2/\text{Co}_3\text{S}_4$ heterojunctions significantly improve the electrocatalytic performance by modifying the electronic structure and enhancing the interaction between the active sites and the H^* intermediates. Benefiting from the above advantages, the resulting P-doped $\text{NiS}_2/\text{Co}_3\text{S}_4@\text{NC}$ catalyst exhibits remarkable electrocatalytic activity with only 150 mV required to drive 10 mA cm^{-2} for HER and 257 mV at 10 mA cm^{-2} for OER in 1 M KOH. This work may offer a promising strategy for the development of highly efficient bifunctional electrocatalysts for water splitting.

2. Experimental section

2.1. Synthesis of NiCo PBA nanocubes

The synthesis of NiCo PBA nanocubes was performed using a coprecipitation method according to our previous work [32,33]. Typically, 12 mmol of $\text{Ni}(\text{NO}_3)_2 \cdot 6\text{H}_2\text{O}$ and 18 mmol of $\text{Na}_3\text{C}_6\text{H}_5\text{O}_7 \cdot 2\text{H}_2\text{O}$ were dissolved in 400 mL of deionized water, referred to as solution A. Separately, 8 mmol of $\text{K}_3[\text{Co}(\text{CN})_6]$ were dissolved in 400 mL of deionized water, referred to as solution B. Solution A was then mixed with solution B and stirred for 30 mins, followed by aging for 24 h. Finally, the resulting NiCo PBA nanocubes were washed several times with deionized water and ethanol and dried overnight at 60°C in a vacuum oven.

2.2. Synthesis of NiCo PBA@PDA

The high-quality NiCo PBA@PDA core-shell nanocubes were prepared by the self-polymerization of dopamine hydrochloride on the surface of NiCo PBA nanocubes. In a typical experiment, 200 mg of the as-synthesized NiCo PBA nanocubes was dispersed in a solution of 40 mL of 0.1 M Tris buffer solution, with a pH of 8.5. The suspension was sonicated to ensure homogeneous dispersion, followed by the addition of 80 mg of dopamine hydrochloride. After that, the mixture was stirred

for 18 h to facilitate the polymerization of dopamine hydrochloride. Finally, the resulting product, denoted as NiCo PBA@PDA, was collected through centrifugation, washed with deionized water and ethanol, and dried under vacuum at 60 °C for 24 h.

2.3. Synthesis of Ni-Co@NC and NiS₂/Co₃S₄@NC

The synthesis procedure of Ni-Co@NC involved the homogeneous dispersion of 200 mg of NiCo PBA@PDA on a porcelain boat, followed by thermal treatment under a N₂ atmosphere at a high temperature of 500 °C for 2 h with a heating rate of 5 °C/min. For the synthesis of NiS₂/Co₃S₄@NC, 50 mg of Ni-Co@NC and 100 mg of sulfur powder were placed in a porcelain boat. The sulfur was positioned in the upper gas outlet and the Ni-Co@NC powder in the lower outlet. The mixture was then subjected to thermal treatment in a N₂-flowing tubular furnace, with a heating rate of 2 °C/min, at 350 °C for 2 h. After the reaction, the sample was naturally cooled to room temperature, the resulting Co₃S₄/NiS₂ heterostructured nanocrystals embedded in N-doped carbon was obtained and designated as NiS₂/Co₃S₄@NC.

2.4. Synthesis of P-NiS₂/Co₃S₄@NC

In a typical synthesis, 500 mg of NaH₂PO₂·H₂O and 20 mg of NiS₂/Co₃S₄@NC powder were placed in a porcelain boat. The NaH₂PO₂·H₂O was positioned in the upper partition, while NiS₂/Co₃S₄@NC powder was placed in the lower partition. The sample was subjected to thermal treatment under a nitrogen atmosphere at 350 °C for 2 h, with a heating rate of 2 °C/min. After cooling to room temperature, the product of P-doped NiS₂/Co₃S₄@NC was obtained.

2.5. Characterizations

The crystal structure and phase of the as-prepared samples were characterized using X-ray Diffraction (XRD) analysis on a D/MAX2200 instrument. The morphological and microstructural characteristics of the samples were examined using Scanning Electron Microscopy (SEM) on a JSM-6700F instrument, Transmission Electron Microscopy (TEM) on a JEM-200CX instrument, and High-Resolution Transmission Electron Microscopy (HRTEM) on a JSM-2010F instrument. A TEM apparatus with an energy dispersive X-ray (EDX) attachment was used to analyze the elemental mapping data of the sample. The composition of the samples was determined using X-ray Photoelectron Spectroscopy (XPS) on a Thermo Scientific K-Alpha + instrument, with a Mono chromated Al-K_α light source. The accurate binding energies were determined by referencing the adventitious C 1 s peak at 284.8 eV. The Raman spectrum of the samples was also obtained using a Renishaw STA409PC instrument and a 532 nm wavelength laser.

2.6. Electrocatalytic measurements

The electrocatalytic performance of the as-synthesized sample was evaluated using a three-electrode setup with a CHI 660e electrochemical workstation. A carbon rod, a standard Hg/HgO electrode, and a nickel foam coated with the catalyst served as the counter electrode, reference electrode, and working electrode, respectively. The preparation of the working electrode involved dispersing 6.0 mg of catalyst in a solution composed of 110 μL of ethanol, 330 μL of water, and 40 μL of naphthol, which was subjected to ultrasonication for 30 mins to obtain a homogeneous dispersion. Subsequently, 120 μL of the mixture was deposited onto a Ni foam substrate (NF, 1 × 1 cm²) and allowed to dry at room temperature. To ensure reliable comparison, the same catalyst loading was used for sulfides-based catalysts, RuO₂, and Pt/C on the NF substrate. All electrochemical measurements, including linear sweep voltammetry (LSVs), cyclic voltammetry (CV), and chronopotentiometry, were performed at room temperature in an O₂-saturated 1.0 M KOH aqueous solution, with 90% iR compensation to eliminate the effect of

solvent resistance. The potential was referenced to the reversible hydrogen electrode (RHE) with the calibration formula: $E_{RHE} = E(Hg/HgO) + 0.0592 \times pH + 0.098$. The long-term stability of the catalyst was monitored in 1.0 M KOH. The electrochemically active surface area (ECSA) was calculated from double-layer capacitance (C_{dl}) measurements, which were obtained from a series of CVs performed at scan rates of 10, 20, 40, 60, 80, and 100 mV·s⁻¹. The double-layer capacitances were acquired by plotting against the scan rates and determining the slopes. The electrochemical impedance spectroscopy (EIS) analysis was performed with the amplitude of 5 mV, the frequency was set in the range of 0.01 Hz–10⁵ Hz.

2.7. Theoretical calculations

Density functional theory (DFT) calculation was performed using the Vienna ab initio simulation packages (VASP) to examine the electronic structure and adsorption properties of the as-prepared catalysts. The generalized gradient approximation (GGA) with the Perdew-Burke-Ernzerh of exchange–correlation functional was employed to describe the exchange and correlation interactions between electrons, with a cut-off energy of 400 eV. The calculation was performed with a convergence threshold of 10⁻⁵ eV for energy and 0.02 eV/Å for force. The Brillouin zone was sampled using the Monkhorst-Pack method with a 2 × 2 × 1 k-point grid. For the DFT calculation of NiS₂, the energetically stable (100) crystal plane was employed, while the (220) crystal plane was used for the calculation of Co₃S₄. The model of NiS₂-Co₃S₄ heterojunction was constructed by first building the (220) surface of Co₃S₄ and the (100) surface of NiS₂, followed by combining the two surfaces in a vacuum slab and optimizing the structure using VASP calculations. The adsorption of hydrogen and water on the interface was studied to provide theoretical evidence for its electrocatalytic performance. The adsorption energies of H were calculated relative to H₂ using the equation $\Delta E = E(\text{slab} + H) - E(\text{slab}) - 1/2E(H_2)$ [34]. The Gibbs free energy of the H adsorption process was expressed as $\Delta G_{H^*} = \Delta E_{H^*} + \Delta ZPE - T\Delta S$, where ΔZPE represents the difference in zero-point energy and ΔS represents the entropy change during H⁺ adsorption.

3. Results and discussion

The synthesis of P-NiS₂/Co₃S₄@NC nanoboxes was carried out following the methodology described in Fig. 1. The synthesis process began with the bottom-up fabrication of uniform and monodispersed NiCo PBA nanocubes at room temperature. Subsequently, a thin and smooth layer of PDA was coated on the surface of the NiCo PBA nanocubes through the self-polymerization of dopamine hydrochloride, thus forming well-defined NiCo PBA@PDA core-shell structures. The nanocubes were then subjected to an annealing treatment at 500 °C for 2 h in a nitrogen atmosphere, which resulted in the conversion of the cyano groups in the PBA and external PDA layer into N-doped carbon. Simultaneously, the internal Ni²⁺ and Co³⁺ ions were reduced to metallic Ni and Co nanoparticles, respectively, which were distributed uniformly within the N-doped carbon nanobox. Subsequently, these individual Ni and Co nanoparticle were transformed into crystalline NiS₂ and Co₃S₄ nanoparticles by a controlling sulfuration reaction. Interestingly, these nanoparticles were closely connected with other by forming heterojunctions. Finally, a phosphation treatment was conducted at 350 °C under nitrogen atmosphere, during which the release of PH₃ gas from the decomposition of NaH₂PO₂·H₂O was reacted with NiS₂ and Co₃S₄, yielding P-doped NiS₂ and P-doped Co₃S₄, respectively. As a result, P-doped NiS₂/Co₃S₄ hetero-nanoparticles embedded in N-doped carbon nanoboxes were successfully synthesized via the pyrolysis-sulfidation-phosphorization strategy.

The morphological and structural features of NiCo PBA templates and resultant products were studied using scanning electron microscopy (SEM) and transmission electron microscopy (TEM). The NiCo PBA nanocubes produced through a facile co-precipitation process were

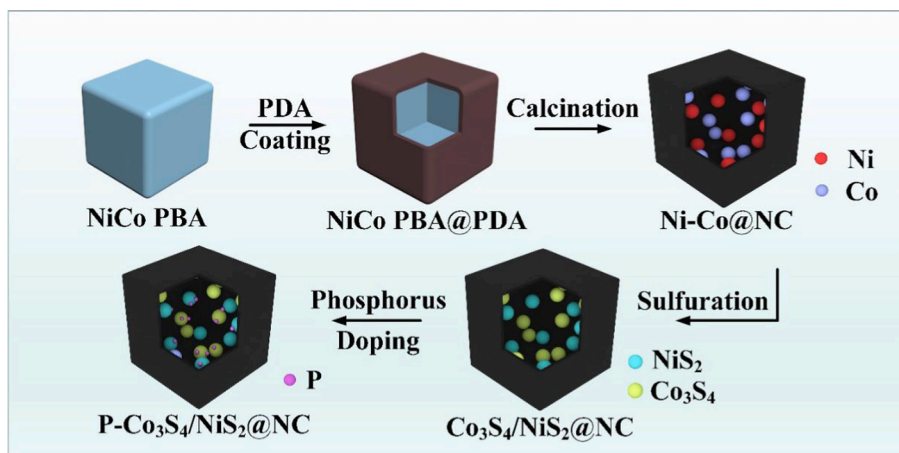


Fig. 1. Schematic illustration of the synthesis of P-NiS₂/Co₃S₄@NC nanobox.

found to be relatively uniform in size with a dimension of 946.1 ± 92.8 nm, as shown in Fig. 2a and Fig. S1. The enlarged SEM image in Fig. 2b revealed a smooth surface for these nanocubes. Additionally, the TEM image in Fig. 2c indicated that these NiCo PBA microcubes were solid in nature. To gain an understanding of the crystallographic structure of the as-obtained NiCo PBA microcubes, X-ray powder diffraction (XRD) analysis was conducted, which confirmed the successful synthesis of Ni-based Prussian blue analogous nanocubes, as indicated by the good agreement between the observed peaks and the simulated patterns (Fig. S2a). The NiCo PBA microcubes were then coated with PDA through immersion in a Tris buffer solution, leading to the formation of NiCo PBA@PDA core-shell microcubes. Although no significant changes in morphology and crystal structure were observed (Fig. 2d–2f and Fig. S2b), the particle size increased to 1028.9 ± 125.9 nm (Fig. S3), indicating the successful coating of a PDA layer on the surface of NiCo

PBA with a thickness of approximately 82 nm. Following the carbonization process, the NiCo PBA@PDA microcubes underwent transformation to become Ni-Co@NC composites. SEM images of Ni-Co@NC, presented in Fig. 2g and 2h, demonstrated that the uniform cube-like morphology was retained, but the size of the nanocubes was decreased obviously. Further analysis through TEM revealed that the organic ligands from the PBA and PDA were effectively converted into carbon, leading to the encapsulation of Ni and Co nanoparticles within the carbon matrix (Fig. 2i). This was corroborated by the XRD results, which exhibited intense diffraction peaks corresponding to metallic cobalt and nickel (Fig. S4).

Due to the high reactivity of the small Ni and Co nanoparticles embedded within a carbon matrix, they are very easy to react with sulfur powder and form corresponding sulfides at elevated temperature. Fig. 3a showed the SEM image of the resultant Co₃S₄-NiS₂@NC sample.

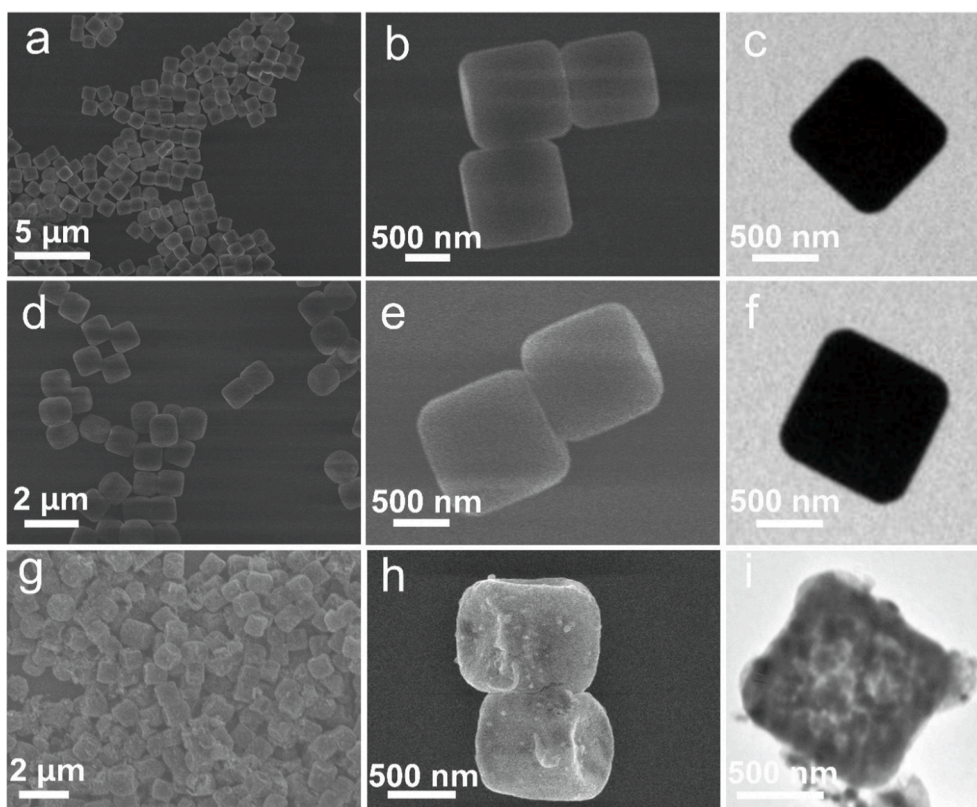


Fig. 2. SEM (a–b, d–e, g–h) and TEM (c, f, i) images of the as-prepared NiCo PBA (a–c), NiCo PBA@PDA (d–f) and Ni-Co@NC (g–i) samples.

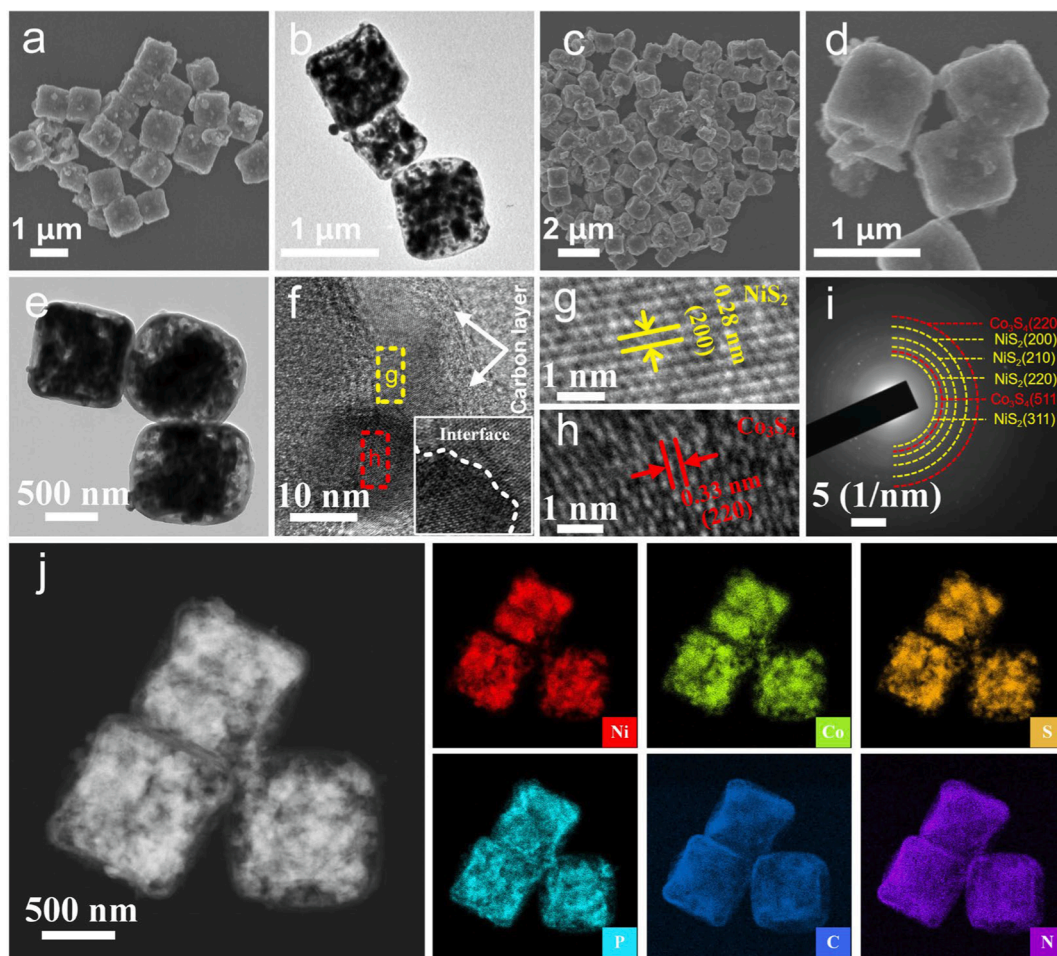


Fig. 3. SEM (a, c), TEM (b, d, e) and HRTEM images (f, g, h) of the as-prepared Co₃S₄/NiS₂@NC (a, b) and P-Co₃S₄/NiS₂@NC (c–h) samples. The SAED (i) and element mapping (j) of the P-Co₃S₄/NiS₂@NC.

It can be seen that its morphology was well preserved. However, TEM image presented in Fig. 3b revealed that it possessed a porous structure, and numerous Co₃S₄ and NiS₂ nanoparticles were uniformly distributed within the carbon matrix. For the P-Co₃S₄-NiS₂@NC nanocubes, the SEM image displayed in Fig. 3c and 3d showed preservation of the cube-like morphology of the NiCo PBA precursor. Whereas, further investigation through TEM revealed the presence of an obvious mesoporous structure within the nanobox, which significantly enhanced the specific surface area for facilitating electrolyte transfer (Fig. 3e). Additionally, close observation showed that P-Co₃S₄-NiS₂ hetero-nanocrystals were uniformly dispersed in the core-shell carbon matrix (Fig. 3f). High-resolution TEM (HRTEM) analysis exhibited well-aligned lattice fringes with lattice spacings of 0.28 nm and 0.33 nm, corresponding to the (200) plane of NiS₂ and the (220) plane of Co₃S₄, respectively (Fig. 3g and 3 h). The existence of Co₃S₄ and NiS₂ are further verified by SAED pattern (Fig. 3i). The element mapping in Fig. 3j confirmed that the P-Co₃S₄-NiS₂@NC nanocubes were primarily composed of Ni, Co, S, P and C elements, which were homogeneously distributed in the entire mesoporous structure.

X-ray diffraction (XRD) measurements were employed to analyze the phase and crystal structures of the as-obtained Co₃S₄/NiS₂@NC and P-doped Co₃S₄/NiS₂@NC samples, as depicted in Fig. 4a. For the Co₃S₄/NiS₂@NC sample, the peaks observed at 2 theta angles of 16.3°, 26.7°, 38.2°, 47.5°, 50.4°, and 55.2° were found to be in agreement with the (111), (220), (400), (422), (511), and (440) planes of Co₃S₄ (JCPDS No. 73–1703), respectively. Additionally, the peaks located at 2 theta angles of 27.2°, 31.5°, 35.3°, 38.8°, 45.1°, and 53.5° matched well with the (111), (200), (210), (211), (220), and (311) facets of NiS₂ (JCPDS

No. 89–3058), respectively. These results confirm that the sample was composed of Co₃S₄ and NiS₂. For the P-Co₃S₄/NiS₂@NC, the position and intensity of the diffraction peaks were found to be largely unchanged. Particularly, no distinct new peak corresponding to phosphides could be observed, indicating the preservation of typical crystal structure of Co₃S₄ and NiS₂. The existence of carbon layer in the samples was confirmed through the use of Raman spectroscopy (Fig. 4b). The presence of D bands at 1350 cm^{−1} and G bands at 1580 cm^{−1}, is evidence of carbon formed through the process of pyrolysis.

The chemical environment and elemental valence of the P-Co₃S₄/NiS₂@NC material were investigated using X-ray photoelectron spectroscopy (XPS). The elements Ni, Co, P, S, C, and O are found in the survey spectra of the sample, as illustrated in Fig. S5. The Ni 2p spectra, as presented in Fig. 4c, were analyzed and revealed the presence of two spin–orbit double peaks, two shakeup satellite peaks, and one peak at 860.1 eV that identified as Ni–P–S. The spin–orbit double peaks at 871.6 eV and 854.0 eV corresponded to Ni²⁺ 2p_{1/2} and Ni²⁺ 2p_{3/2}, respectively. Whereas the second pair at 875.4 eV and 856.7 eV were attributed to Ni³⁺ 2p_{1/2} and Ni³⁺ 2p_{3/2}, respectively. Additionally, the satellite peaks (denoted as Sat.) were observed at 880.2 eV and 863.7 eV. For the Co 2p, the peaks at 798.4 eV and 782.3 eV were assigned to Co²⁺ 2p_{1/2} and Co²⁺ 2p_{3/2}, and Co³⁺ 2p_{1/2} and Co³⁺ 2p_{3/2} at 794.1 eV and 779.0 eV, respectively (Fig. 4d). The Co 2p satellite peaks were observed at 803.4 eV and 786.2 eV, in agreement with previous reports [35]. The XPS spectrum of P 2p, as presented in Fig. 4e, were analyzed and revealed a peak at 134.3 eV, which was attributed to P–O due to unavoidable oxidation [36]. The two peaks at 130.5 and 128.8 eV can be assigned to P 2p_{1/2} and P 2p_{3/2}, respectively. The XPS patterns of S 2p,

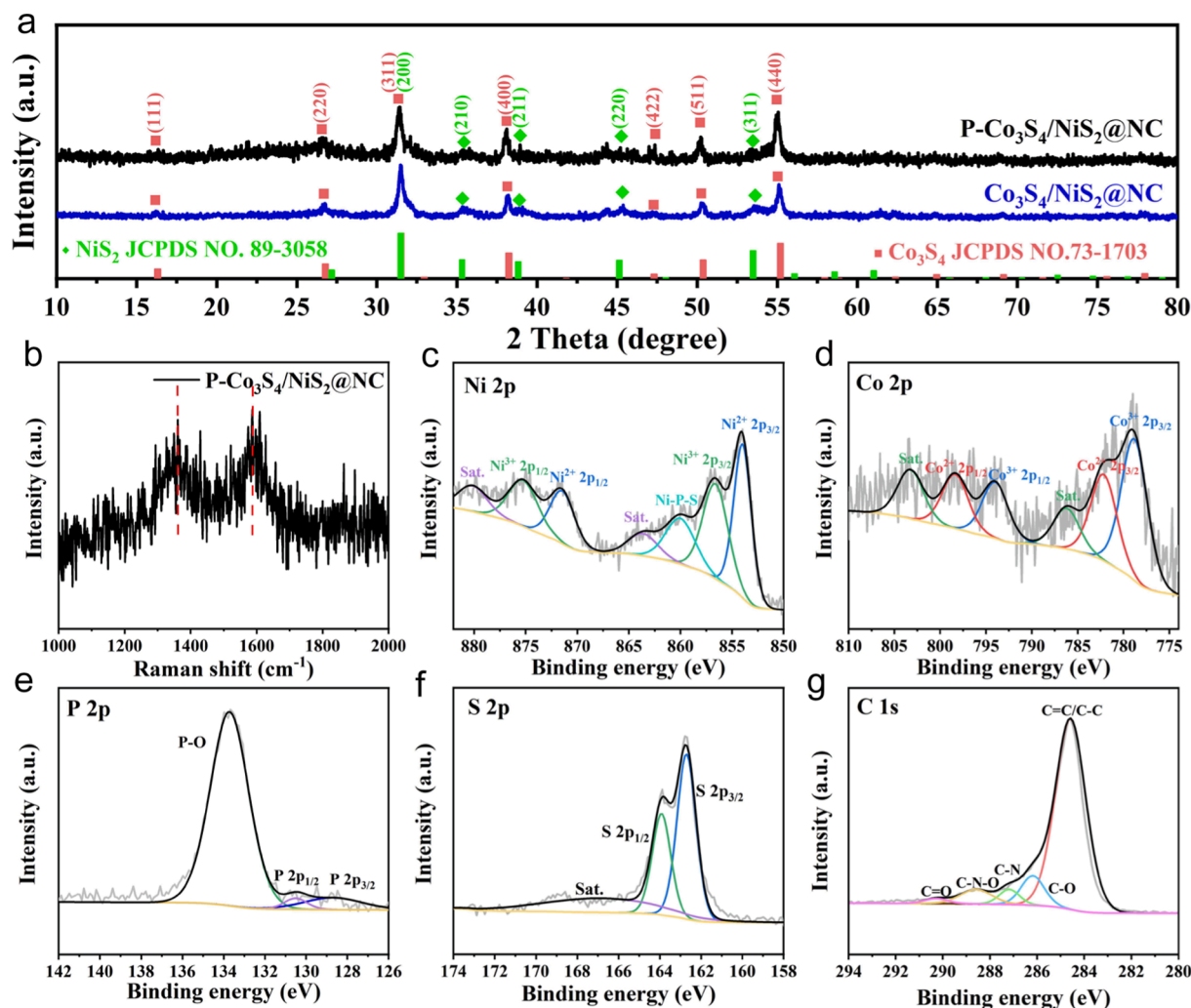


Fig. 4. XRD patterns (a) of the as-synthesized Co₃S₄/NiS₂@NC sample and P-Co₃S₄/NiS₂@NC sample. Raman spectrum (b) and XPS spectrum (c-g) of the P-Co₃S₄/NiS₂@NC sample: (c) Ni 2p; (d) Co 2p; (e) P 2p; (f) S 2p; (g) C 1s.

as shown in Fig. 4f, exhibited peaks at 163.9 eV and 162.7 eV, which corresponded to S 2p_{1/2} and S 2p_{3/2}, respectively [37]. From the XPS spectrum in Fig. 4g, the fitted C 1s spectrum can be observed to have a primary peak at around 284.6 eV, which corresponds to the C=C/C-C bonds. The peaks at 286.2, 287.1, 288.5 and 290.2 eV can be ascribed to the C-O, C-N, C-N-O and C=O bonds, respectively [38].

The electrocatalytic performance of the as-synthesized samples toward HER was evaluated using a standard three-electrode system in a 1.0 M KOH electrolyte. The linear sweep voltammetry (LSV) curves for each catalyst are presented in Fig. 5a. The NiCo PBA nanocubes exhibited a low electrocatalytic activity with a high η_{10} of 234 mV, which can be attributed to its low conductivity and limited catalytic active sites. In comparison, the Ni-Co@NC showed an improvement in HER performance, with an η_{10} of 201 mV. Particularly, the incorporation of P dopant into the Co₃S₄/NiS₂@NC resulted in a remarkable improvement in HER behavior, as evident from the lower η_{10} value of 150 mV, which is much smaller than the Co₃S₄/NiS₂@NC sample (180 mV). These results indicate that the presence of P enhances the electronic structure of the catalyst, activates HER reaction and promotes the generation of H₂ gas. Although the HER activity of P-Co₃S₄/NiS₂@NC is not as high as that of the 20 wt% Pt/C catalyst, it is comparable to or better than most cobalt- and nickel-based sulfides (Table S1). To effectively highlight the improvements brought by P-doping and Co₃S₄-NiS₂ hetero-interface on the HER electrocatalytic activity, NiS₂@NC, P-NiS₂@NC, Co₃S₄@NC and P-Co₃S₄@NC were also prepared using NiNi

and CoCo PBA as precursors, respectively. As shown in Fig. S6 and Fig. S7, it is obvious that they are very similar to the precursors in shape and structure. However, the HER performance of these catalysts was much worse than that of P-Co₃S₄-NiS₂@NC (Fig. S8), demonstrating that the formation of Co₃S₄-NiS₂ heterostructures associated with P-doping improved the intrinsic activity of the catalysts, resulting in the excellent HER electrocatalytic activity of P-Co₃S₄-NiS₂@NC. To gain insight into the rate-determining step of the HER process, Tafel plots were analyzed (Fig. 5b) [39]. The overpotentials at 10 mA cm⁻² (η_{10}), 50 mA cm⁻² (η_{50}), and the corresponding Tafel slopes of different catalysts are summarized and displayed in Fig. 5c. The Tafel slope of P-Co₃S₄/NiS₂@NC (115.91 mV dec⁻¹) was found to be lower than those of NiCo PBA (148.84 mV dec⁻¹), Ni-Co@NC (147.52 mV dec⁻¹), and Co₃S₄/NiS₂@NC (129.57 mV dec⁻¹), respectively. The lower η_{10} and Tafel slopes indicated that the P-Co₃S₄/NiS₂@NC had better HER performance.

The electrochemically active surface areas of the as-fabricated catalysts were analyzed to gain more insights into their different electrochemical behaviors. Cyclic voltammograms (CV) measurements were performed in the non-Faradaic regions with different scan rates to estimate the electrochemical double-layer capacitance (C_{dl}), which is proportional to the electrochemical active surface area (ECSA) [40,41]. As evidenced by the CV curves in Fig. S9, the C_{dl} values of NiCo PBA, Ni-Co@NC, Co₃S₄/NiS₂@NC, and P-Co₃S₄/NiS₂@NC were calculated to be 6.75, 6.93, 11.82, and 14.20 mF cm⁻², respectively (Fig. 5d). The larger C_{dl} value of P-Co₃S₄/NiS₂@NC suggests that it can provide more

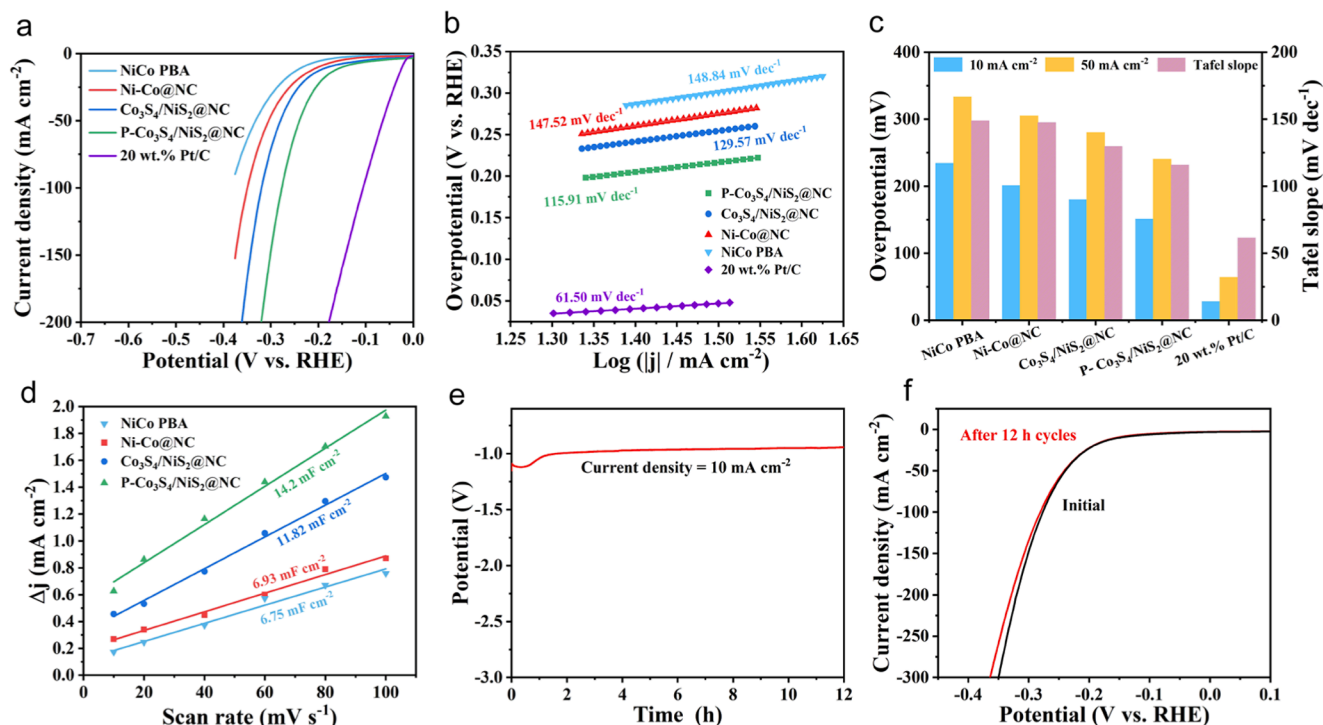


Fig. 5. HER performances in 1 M KOH. LSV curves (a), Tafel plots (b), the summary of η_{10} , η_{50} and Tafel slopes (c) of NiCo PBA, Ni-Co@NC, Co₃S₄/NiS₂@NC, P-Co₃S₄/NiS₂@NC and 20 wt.% Pt/C; The C_{dl} (d); Stability test of P-Co₃S₄/NiS₂@NC by keeping the current density of 10 mA cm⁻² for 12 h (e) and LSV curves before and after 12 h cycles (f).

electrocatalytic active sites for HER, indicating that P-doping effectively increase the electrochemically active surface area. The HER stability of the P-Co₃S₄/NiS₂@NC catalyst was evaluated through long-term chronopotentiometry and the results are displayed in Fig. 5e. After 1 h of

activation at a constant current of 10 mA cm⁻², the voltage required only decreased from 1.11 V to 0.95 V and remained stable at that potential. In addition, LSV plots were measured before and after a 12-hour stability test, and as illustrated in Fig. 5f, only a minor decline trend was

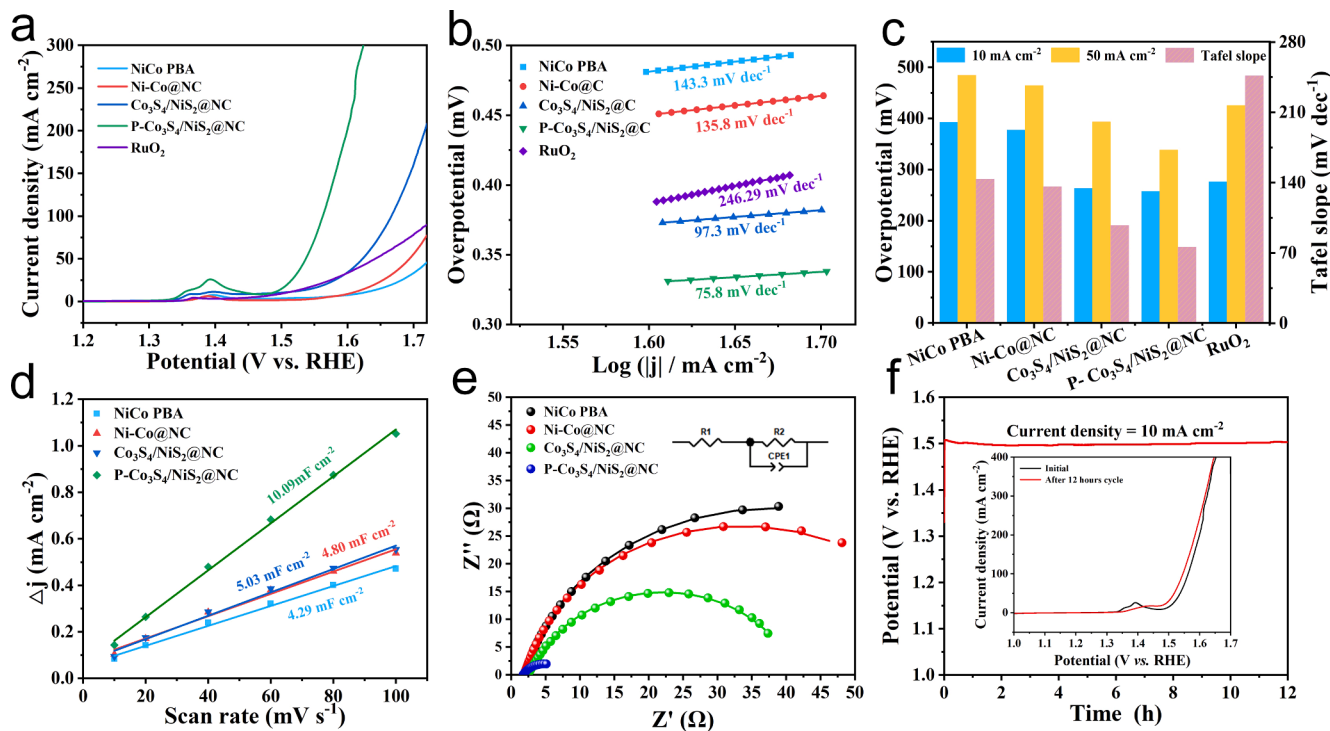


Fig. 6. OER performances in 1 M KOH. LSV curves (a), Tafel plots (b), the summary (c) of η_{10} , η_{50} and Tafel slopes of NiCo PBA, Ni-Co@NC, Co₃S₄/NiS₂@NC, P-Co₃S₄/NiS₂@NC and RuO₂; The C_{dl} values (d), the EIS spectrum (e) and stability test (f) of P-Co₃S₄/NiS₂@NC by keeping the current density of 10 mA cm⁻² for 12 h and LSV curves (f) before and after 12 h cycles.

observed, indicating the good stability of P-Co₃S₄/NiS₂@NC in alkaline solution. Furthermore, after a 36-hour stability test, P-Co₃S₄/NiS₂@NC still exhibited stable and efficient performance for HER during the entire test, as shown in Fig. S10. To compare the morphological, crystal structure and compositional changes of the P-Co₃S₄/NiS₂@NC catalyst before and after the HER stability test, SEM, and XRD measurements were carried out. Following the HER test, the SEM image of P-Co₃S₄/NiS₂@NC reveals morphological agglomeration and increasing roughness (Fig. S11a). Fig. S11b displayed the XRD result, the strong peaks at 44.7°, 52.0°, and 76.6° are the Ni peaks of nickel foam, and the post-HER sample exhibits imperceptible peak changes or shifts, confirming the excellent stability of P-Co₃S₄/NiS₂@NC for HER in alkaline solution.

The OER electrocatalytic performance of the as-formed catalysts was also evaluated in a 1 M KOH solution using commercial RuO₂ as a reference. The electrochemical performance for all the samples was compared in Fig. 6a and Fig. S12. The commercial RuO₂ required 276 mV to drive 10 mA cm⁻², which was consistent with the reports elsewhere [42], indicating the valid measurement techniques. Additionally, a small peak was present at 1.41 V for all the catalysts, which can be attributed to the redox reaction of Ni²⁺/Ni³⁺ [43]. To afford a current density of 10 mA cm⁻², the required overpotentials for the NiCo PBA, Ni-Co@NC, Co₃S₄/NiS₂@NC, Co₃S₄@NC, NiS₂@NC, P-Co₃S₄@NC, P-NiS₂@NC and P-Co₃S₄/NiS₂@NC catalysts were found to be 392, 377, 263, 315, 326, 271, 307 and 257 mV, respectively, signifying the remarkable OER catalytic activity of P-Co₃S₄/NiS₂@NC. Of particular interest was the observation that the P-Co₃S₄/NiS₂@NC displayed a lower overpotential of 338 mV at a current density of 50 mA cm⁻², much lower than that of RuO₂ catalyst (412 mV). In addition, as illustrated in Fig. 6b, the P-Co₃S₄/NiS₂@NC exhibited the lowest Tafel slope of 75.8 mV dec⁻¹ among the electrocatalysts investigated, i.e., 143.3 mV dec⁻¹ for NiCo PBA, 135.8 mV dec⁻¹ for Ni-Co@NC, and 97.3 mV dec⁻¹ for Co₃S₄/NiS₂@NC. For clarity, the specific overpotentials and corresponding Tafel slope for different catalysts were illustrated in Fig. 6c. One can find that the catalytic activity of P-Co₃S₄/NiS₂@NC was not only super to NiCo PBA and Co₃S₄/NiS₂@NC but also outperformed many other reported non-noble catalysts (Table S2). The enhanced intrinsic activity for OER can be attributed to its favorable morphology, structure and composition. Derived from the CV plots measured in the non-Faradaic region, the extracted C_{dl} values of P-Co₃S₄/NiS₂@NC, NiCo PBA, Ni-Co@NC, Co₃S₄/NiS₂@NC were 10.09, 4.29, 4.80, and 5.03 mF cm⁻², respectively (Fig. 6d and Fig. S13). As compared to Co₃S₄/NiS₂@NC, the higher C_{dl} value of P-Co₃S₄/NiS₂@NC was beneficial for the increase and exposure of active sites, contributing to the penetration of electrolytes, and facilitating the OER process. Electrochemical impedance (EIS) measurements were carried out to comprehend the electrochemical process and reaction kinetics on electrode surface. It is widely known that the charge transfer resistance (R_{ct}) is an important parameter for illuminating the charge transfer kinetics at the catalyst/electrolyte interface [44]. The EIS plots (Fig. 6e) and Table S3 showed that P-Co₃S₄/NiS₂@NC had a lower charge transfer resistance than NiCo PBA, Ni-Co@NC, and Co₃S₄/NiS₂@NC, demonstrating that electronic modulation by interfacial engineering was a successful method for boosting the activity of OER electrocatalysts. Additionally, the P-Co₃S₄/NiS₂@NC was assessed for its OER stability using a chronopotentiometric method. Fig. 6f shows that the potential remained constant at around 1.54 V when the electrode was subjected to a current density of 10 mA cm⁻², demonstrating that P-Co₃S₄/NiS₂@NC could sustain stable electrocatalytic activity for OER in an alkaline solution. Following a 12-hour and 36-hour stability test, the LSV of the material was re-examined, as shown in Fig. 6f and Fig. S14. The results indicate that the OER catalytic activity of P-Co₃S₄/NiS₂@NC decreased after the long-term stability test, which can be attributed to structural and physical phase changes that occurred during the OER process [23,24,45].

To further explore the actual active species of the P-Co₃S₄/NiS₂@NC during the OER process, the SEM, XRD, and XPS characterizations were

carried out after long-term test. As seen in Fig. S15a, the oxidation of P-Co₃S₄/NiS₂@NC surface was probably the cause of the surface becoming rough. The XRD patterns revealed that the peaks of Co₃S₄ and NiS₂ were still visible after the OER reaction (Fig. S15b), but intensities of the peaks decreased, indicating that the material has partially undergone phase transformation of Co₃S₄ with NiS₂ after 12 h OER. As shown in Fig. S15c, Ni 2p of the catalyst shows the appearance of new peaks with binding energies of 861.1 eV that may be attributed to Ni-O after OER, showing that the metal elements on the surface of catalyst have undergone partial oxidation. However, the Co 2p XPS shows that the peaks the Co species were apparently reduced or disappeared indicating the surface Co species might be oxidized during the OER process (Fig. S15d). the XPS signal of P 2p (Fig. S15e) was invisible as the consequence after 12 h of OER, proving that the phosphorus doped in the material was effortless to lost during the reaction process led to the content decreases [46]. In the XPS spectrum of S 2p in Fig. S15f, a new peak appeared at 169.4 eV for the oxidation of sulfur, revealing that the surface sulfide had been partially converted to sulfur oxides. These findings show that during the OER activation process, the surface of P-Co₃S₄/NiS₂@NC nanoplates was largely oxidized to OER-active oxyhydroxides and reached the stable state.

For the sake of exploring the bifunctional feature toward overall water-splitting, a two-electrode system is assembled in 1 M KOH electrolyte. As can be shown from Fig. 7a, P-doped Co₃S₄/NiS₂@NC only needs a cell voltage of 1.59 V to produce 10 mA cm⁻² in 1 M KOH, demonstrating the superiority of synergistically control by fusing heterojunction with the P-doping effect. Large amounts of H₂ and O₂ bubbles emitted from the surface of cathode and anode during the electrolysis process also served as further evidence of exceptional overall water splitting capability of the P-Co₃S₄/NiS₂@NC sample (Fig. 7b). The chronopotentiometry curves in Fig. 7c show that the optimized P-doped Co₃S₄/NiS₂@NC sample may operate well for a period of 24 h at 10 mA cm², indicating its outstanding stability.

Density functional theory (DFT) calculations were then performed to gain insights into the roles of P-doping and Co₃S₄-NiS₂ heterojunctions for the enhanced HER performance. The Gibbs free energy change of the adsorbed H ($|\Delta G_{H^*}|$), commonly used to evaluate the HER activity of a catalyst, was calculated for H adsorption on the surface of Co₃S₄, NiS₂ and P-Co₃S₄/NiS₂ heterojunctions [47]. The crystal structure of NiS₂ and Co₃S₄ are displayed in Fig. 8a and 8b, respectively. The structure model of P-NiS₂/Co₃S₄ with optimized spacing was displayed in Fig. S16, and the optimized structures of H* adsorbed on the surface of P-Co₃S₄-NiS₂ heterojunction, P-NiS₂ and P-Co₃S₄ are shown in Fig. 8c-8d and Fig. S17, respectively. As is well known, an ideal catalyst for H binding should exhibit moderate H adsorption free energy close to thermo-neutral ($|\Delta G_{H^*}| \approx 0$), as the HER relies on the reversible adsorption and desorption of H. As shown in Fig. 8e, ΔG_{H^*} of H adsorption on the Ni sites of NiS₂, P-NiS₂, Co₃S₄/NiS₂ and P-Co₃S₄/NiS₂ were found to be 0.82, 0.64, 0.33 eV and 0.28 eV, respectively. However, ΔG_{H^*} of the P-Co₃S₄-NiS₂ catalyst dramatically changed to 0.02 eV for the Co site, close to the ideal ΔG_{H^*} of 0 eV for the catalyst-H* state, suggesting its outstanding HER catalytic performance. Notably, the ΔG_{H^*} of H adsorption on the Co sites of Co₃S₄ also decreased after P-doping. Additionally, it was found that substituting an S atom with a P atom at the P site could reduce the ΔG_{H^*} value to -0.19 eV in the P-Co₃S₄/NiS₂, revealing that the doping of P could be served as the new active sites. In alkaline media, the adsorption of H₂O is significant for water dissociation on a catalyst surface for HER and OER [48]. The H₂O adsorption energy (ΔE_{H_2O}) was calculated on these surfaces, and the results are presented in Fig. 8g. The P-Co₃S₄-NiS₂ exhibited a lower H₂O adsorption energy value of -0.96 eV than that of NiS₂ (-0.37 eV), P-NiS₂ (-0.42 eV) and Co₃S₄/NiS₂ (-0.78 eV), indicating higher H₂O binding activity and thus guaranteed effective water adsorption. Furthermore, as shown in Fig. 8h, the calculated density of states (DOS) revealed that the Co₃S₄-NiS₂ heterostructure was in a metallic state with enhanced carrier density near the Fermi level, compared to that of P-NiS₂ and P-Co₃S₄. The higher electron density at

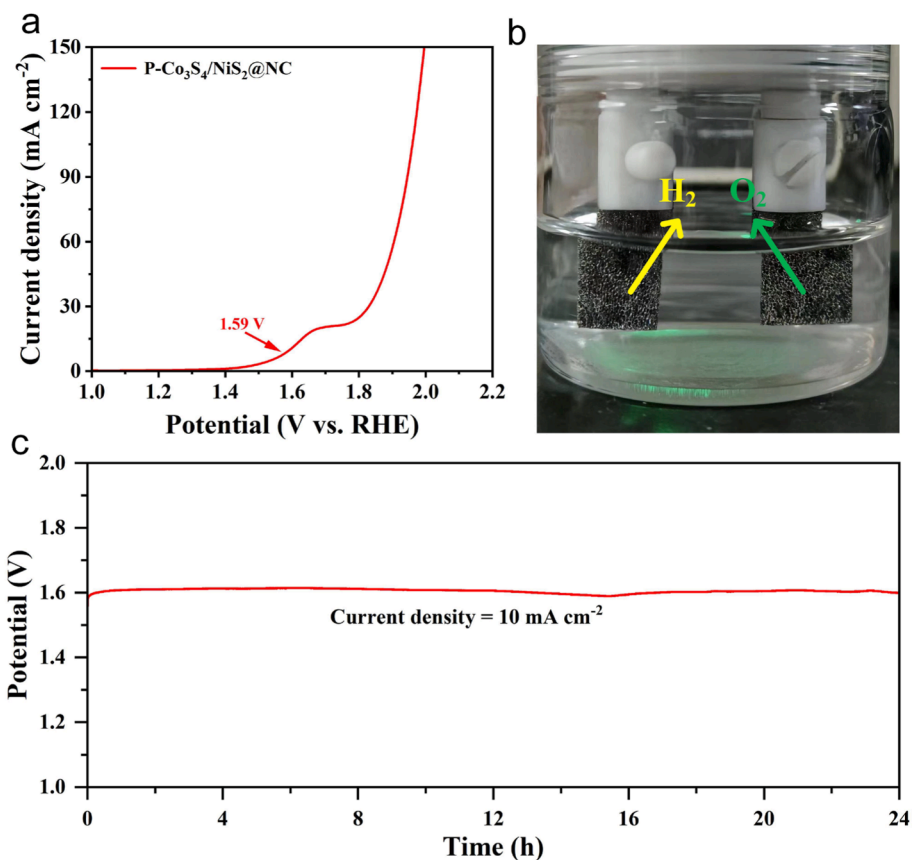


Fig. 7. (a) Polarization curves of the P-Co₃S₄/NiS₂@NC sample for overall water splitting in a two-electrode configuration. (b) The digital photograph of the anode and cathode during the water splitting process. (c) The chronopotentiometry curve of P-Co₃S₄/NiS₂@NC for water electrolysis at 10 mA cm⁻² in 1.0 M KOH.

the Fermi level led to higher electrical conductivity, contributing to the enhanced electrochemical performance due to elevated electron transfer [49]. The charge density differences in Fig. 8i demonstrate a self-driven electron transfer from P-doped NiS₂ (100) to P-doped Co₃S₄ (220), indicating a strong charge exchange occurred between the two materials. The calculated work function for P-NiS₂ and P-Co₃S₄, as shown in Fig. 8j and Fig. S18, confirms this observation, with values of ~4.96 and 5.11 eV, respectively. Therefore, the interface charge will spontaneously transfer from P-NiS₂ to P-Co₃S₄ across their contact interface, resulting in interfacial electron redistribution until the work function equilibrium is reached. These results emphasize the crucial role of P-doping and heterojunctions in inducing electron redistribution, which can provide continuous electron transport across the interface to facilitate the electrochemical process, and effectively optimize the electronic structure of Co and Ni centers to accelerate the reaction kinetics.

Based on the above results, the exceptional electrocatalytic activity of P-doped Co₃S₄/NiS₂@NC nanoboxes for both HER and OER can be primarily attributed to several key factors. Firstly, the unique hollow structure of the nanomaterial and the nanoparticles contained within it result in a high specific surface area, which provides an abundance of available active sites for catalytic reactions. Secondly, the introduction of P into the Co₃S₄ and NiS₂ components significantly increases the conductivity and number of active sites, thereby enhancing the overall catalytic activity. Thirdly, the formation of a heterojunction between Co₃S₄ and NiS₂ promotes the redistribution of electrons, facilitating electron transfer kinetics and further enhancing the intrinsic activity of the catalyst. Lastly, the carbon matrix surrounding the Co₃S₄/NiS₂ nanoparticles not only protects them from corrosion but also acts as a conductive pathway for efficient electron transfer.

4. Conclusions

In summary, we have successfully synthesized P-doped NiS₂/Co₃S₄ hetero-nanoparticles embedded in N-doped carbon nanoboxes through a typical pyrolysis-sulfidation-phosphorization strategy. The resulting material exhibited remarkable electrocatalytic activity and stability towards both HER and OER in alkaline solutions. Particularly, the OER overpotential was found to be only 257 mV, enabling a current density of 10 mA cm⁻² in 1 M KOH. The exceptional performance of the material was attributed to the enhanced conductivity and active sites as well as synergistic effects between NiS₂ and Co₃S₄. Theoretical simulations were performed to further understand the electronic structure and H and H₂O adsorption behavior of the system, and it was found that P-doping and strong coupling interactions between NiS₂ and Co₃S₄ were key to optimizing the electrocatalytic activity. This study provides new insights into the design and synthesis of low-cost and highly active transition metal-based electrode materials for various electrocatalysis applications.

CRedit authorship contribution statement

Shoushuang Huang: Conceptualization, Investigation, Formal analysis, Funding acquisition, Supervision, Validation. **Shuzhen Ma:** Writing – review & editing, Investigation, Formal analysis. **Libin Liu:** Investigation, Methodology, Writing – review & editing. **Zhiqiang Jin:** Data curation, Formal analysis, Resources. **Pengyan Gao:** Investigation, Formal analysis, Resources, Validation. **Kaimei Peng:** Resources, Conceptualization, Funding acquisition, Project administration. **Yong Jiang:** Conceptualization, Formal analysis. **Amene Naseri:** Conceptualization. **Zhangjun Hu:** Conceptualization, Investigation, Writing – original draft. **Jiujun Zhang:** Writing – review & editing, Resources,

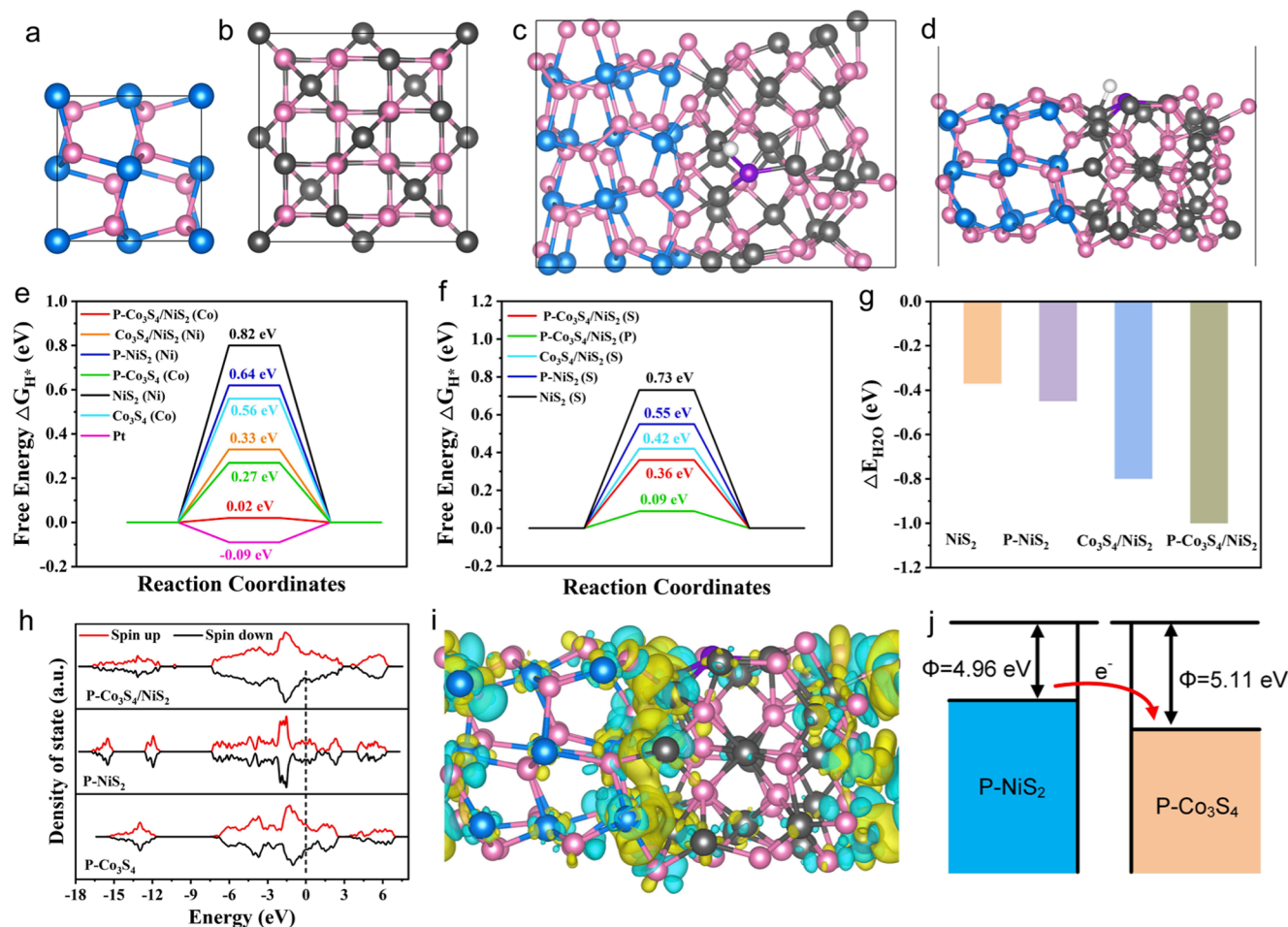


Fig. 8. The crystal structure of NiS₂ (a) and Co₃S₄ (b). Top (c) and side (d) view of the optimized geometry of P-Co₃S₄/NiS₂ for hydrogen adsorption. HER free energy diagram (e-f) and adsorption energy (g) on the catalyst with different sites. (h) Calculated electronic density of states (DOS). (i) Charge density difference of P-Co₃S₄/NiS₂; (j) Energy band diagram of P-Co₃S₄ and P-NiS₂. The blue, pink, black, and purple represent the elements of nickel, sulfur, cobalt and phosphorus, respectively.

Conceptualization.

Declaration of Competing Interest

The authors declare that they have no known competing financial interests or personal relationships that could have appeared to influence the work reported in this paper.

Data availability

Data will be made available on request.

Acknowledgments

The work was financially supported by the National Natural Science Foundation of China (12275168), Science and Technology Innovation Plan of Shanghai Science and Technology Commission (21010500300), Guizhou Provincial Science and Technology Foundation (No. [2020] 1Y043), STINT Joint China-Sweden Mobility Project (CH2017-7243), and Swedish Government Strategic Research Area in Materials Science on Advanced Functional Materials at Linköping University (SFO-Mat-LiU, No. 2009-0097).

Appendix A. Supplementary data

Supplementary data to this article can be found online at <https://doi.org/10.1016/j.jcis.2023.08.092>.

References

- [1] H. Dotan, A. Landman, S.W. Sheehan, K.D. Malviya, G.E. Shter, D.A. Grave, Z. Arzi, N. Yehudai, N. Halabi, N. Gal, N. Hadari, C. Cohen, A. Rothschild, G.S. Grader, Decoupled hydrogen and oxygen evolution by a two-step electrochemical-chemical cycle for efficient overall water splitting, *Nat. Energy* 4 (2019) 786–795, <https://doi.org/10.1038/s41560-019-0462-7>.
- [2] Z.X. Li, C.C. Yu, Y.K. Kang, X. Zhang, Y.Y. Wen, Z.K. Wang, C. Ma, C. Wang, K.W. Wang, X.L. Qu, M. He, Y.W. Zhang, W.Y. Song, Ultra-small hollow ternary alloy nanoparticles for efficient hydrogen evolution reaction, *Nat. Sci. Rev.* 8 (2021) nwaa204, <https://doi.org/10.1093/nsr/nwaa204>.
- [3] G.Q. Zhao, K. Rui, S.X. Dou, W.P. Sun, Heterostructures for Electrochemical Hydrogen Evolution Reaction: A Review, *Adv. Funct. Mater.* 28 (2018) 1803291, <https://doi.org/10.1002/adfm.201803291>.
- [4] Q.B. Wu, J.W. Liang, M.J. Xiao, C. Long, L. Li, Z.H. Zeng, A. Mavrić, X. Zheng, J. Zhu, H.W. Liang, H.F. Liu, M. Valant, W. Wang, Z.X. Lv, J. Li, C.H. Cui, Non-covalent ligand-oxide interaction promotes oxygen evolution, *Nat. Commun.* 14 (2023) 997, <https://doi.org/10.1038/s41467-023-36718-3>.
- [5] Y.X. Qi, T.T. Li, Y.J. Hu, J.H. Xiang, W.Q. Shao, W.H. Chen, X.Q. Mu, S.L. Liu, C. Y. Chen, M. Yu, S.C. Mu, Single-atom Fe Embedded Co₃S₄ for Efficient Electrocatalytic Oxygen Evolution Reaction, *Chem. Res. Chinese U.* 38 (2022) 1282–1286, <https://doi.org/10.1007/s40242-022-2248-x>.
- [6] X.F. Lu, S.L. Zhang, W.L. Sim, S.Y. Gao, X.W. Lou, Phosphorized CoNi₂S₄ Yolk-Shell Spheres for Highly Efficient Hydrogen Production via Water and Urea Electrolysis, *Angew. Chem. Int. Ed.* 60 (2021) 22885–22891, <https://doi.org/10.1002/anie.202108563>.
- [7] X.Y. Gu, S.S. Li, W.Q. Shao, X.Q. Mu, Y.X. Yang, Y. Ge, W.T. Meng, G.X. Liu, S. L. Liu, S.C. Mu, Cation/Anion Dual-Vacancy Pair Modulated Atomically-Thin Se_x-Co₃S₄ Nanosheets with Extremely High Water Oxidation Performance in Ultralow-Concentration Alkaline Solutions, *Small* 18 (2022) 202108097, <https://doi.org/10.1002/smll.202108097>.
- [8] I.S. Kwon, I.H. Kwak, J.Y. Kim, T.T. Debela, Y.C. Park, J. Park, H.S. Kang, Concurrent Vacancy and Adatom Defects of Mo_{1-x}Nb_xSe₂ Alloy Nanosheets Enhance Electrochemical Performance of Hydrogen Evolution Reaction, *ACS Nano* 15 (2021) 5467–5477, <https://doi.org/10.1021/acsnano.1c00171>.

- [9] X. Luo, P.X. Ji, P.Y. Wang, X. Tan, L. Chen, S.C. Mu, Spherical $\text{Ni}_3\text{S}_2/\text{Fe-NiP}_x$ Magic Cube with Ultrahigh Water/Seawater Oxidation Efficiency, *Adv. Sci.* 9 (2022) 2104846, <https://doi.org/10.1002/adv.202104846>.
- [10] J.W. Li, Y.Z. Hu, X. Huang, Y. Zhu, D.L. Wang, Bimetallic Phosphide Heterostructure Coupled with Ultrathin Carbon Layer Boosting Overall Alkaline Water and Seawater Splitting, *Small* 19 (2023) 2206533, <https://doi.org/10.1002/sml.202206533>.
- [11] J.P. Chen, B.W. Ren, H. Cui, C.X. Wang, Constructing Pure Phase Tungsten-Based Bimetallic Carbide Nanosheet as an Efficient Bifunctional Electrocatalyst for Overall Water Splitting, *Small* 16 (2020) 1907556, <https://doi.org/10.1002/sml.201907556>.
- [12] M. Feng, J.L. Huang, Y. Peng, C.R. Huang, X. Yue, S.M. Huang, Tuning Electronic Structures of Transition Metal Carbides to Boost Oxygen Evolution Reactions in Acidic Medium, *ACS Nano* 16 (2022) 13834–13844, <https://doi.org/10.1021/acsnano.2c02099>.
- [13] T. Kavinkumar, H. Yang, A.T. Sivagurunathan, H. Jeong, J.W. Han, D.H. Kim, Regulating Electronic Structure of Iron Nitride by Tungsten Nitride Nanosheets for Accelerated Overall Water Splitting, *Small* (2023) 2300963, <https://doi.org/10.1002/sml.202300963>.
- [14] Z.N. Zahran, E.A. Mohamed, Y. Tsubonouchi, M. Ishizaki, T. Togashi, M. Kurihara, K. Saito, T. Yui, M. Yagi, Electrocatalytic water splitting with unprecedentedly low overpotentials by nickel sulfide nanowires stuffed into carbon nitride scabbards, *Energ. Environ. Sci.* 14 (2021) 5358–5365, <https://doi.org/10.1039/d1ee00509j>.
- [15] Y.N. Guo, T. Park, J.W. Yi, J. Henzie, J. Kim, Z.L. Wang, B. Jiang, Y. Bando, Y. Sugahara, J. Tang, Y. Yamauchi, Nanoarchitectonics for Transition-Metal-Sulfide-Based Electrocatalysts for Water Splitting, *Adv. Mater.* 31 (2019) 1807134, <https://doi.org/10.1002/adma.201807134>.
- [16] L. Zhang, X. Gao, Y. Zhu, A. Liu, H. Dong, D. Wu, Z. Han, W. Wang, Y. Fang, J. Zhang, Z. Kou, B. Qian, T.T. Wang, Electrocatalytically inactive copper improves the water adsorption/dissociation on Ni_3S_2 for accelerated alkaline and neutral hydrogen evolution, *Nanoscale* 13 (2021) 2456–2464, <https://doi.org/10.1039/d0nr07275c>.
- [17] M.H. Wu, W.J. Chou, J.S. Huang, D.B. Putungan, S.H. Lin, First-principles investigation of the hydrogen evolution reaction on different surfaces of pyrites MnS_2 , FeS_2 , CoS_2 , NiS_2 , *PCCP* 21 (2019) 21561–21567, <https://doi.org/10.1039/c9cp03893k>.
- [18] B. Zhang, X.L. Fu, L. Song, X.J. Wu, Surface selectivity of Ni_3S_2 toward hydrogen evolution reaction: a first-principles study, *PCCP* 22 (2020) 25685–25694, <https://doi.org/10.1039/d0cp03845h>.
- [19] Y.T. Li, T.Y. Dai, Q.X. Wu, X.Y. Lang, L.J. Zhao, Q. Jiang, Design heterostructure of NiS-NiS_2 on NiFe layered double hydroxide with Mo doping for efficient overall water splitting, *Mater. Today Energy* 23 (2022), <https://doi.org/10.1016/j.mtener.2021.100906>.
- [20] H. Liu, J.N. Cheng, W.J. He, Y. Li, J. Mao, X.R. Zheng, C. Chen, C.X. Cui, Q.Y. Hao, Interfacial electronic modulation of Ni_3S_2 nanosheet arrays decorated with Au nanoparticles boosts overall water splitting, *Appl. Catal. B-Environ* 304 (2022), 120935, <https://doi.org/10.1016/j.apcatb.2021.120935>.
- [21] J. Wu, Q. Zhang, K. Shen, R. Zhao, W.D. Zhong, C.F. Yang, H. Xiang, X.K. Li, N. J. Yang, Modulating Interband Energy Separation of Boron-Doped $\text{Fe}_3\text{S}_4/\text{FeS}_2$ Electrocatalysts to Boost Alkaline Hydrogen Evolution Reaction, *Adv. Funct. Mater.* 32 (2022) 2107802, <https://doi.org/10.1002/adfm.202107802>.
- [22] L.M. Zhao, Y.F. Tong, Y.P. Ding, W.C. Kong, J.J. Wang, B.Y. Li, Y.C. Zhen, J. Xu, W. Xing, Designing interface structures of nickel with transition metal nitrides for enhanced hydrogen electro-oxidation, *Surf. Interfaces* 37 (2023), 102659, <https://doi.org/10.1016/j.surfin.2023.102659>.
- [23] X.R. Li, C.L. Wang, S.S. Zheng, H.G. Xue, Q. Xu, P. Braunstein, H. Pang, Electrochemical activation-induced surface-reconstruction of NiOx microbelt superstructure of core-shell nanoparticles for superior durability electrocatalysis, *J. Colloid Interface Sci.* 624 (2022) 443–449, <https://doi.org/10.1016/j.jcis.2022.05.160>.
- [24] P.L. Zhai, C. Wang, Y. Zhao, Y.Y. Zhang, J.F. Gao, L.C. Sun, J.G. Hou, Regulating electronic states of nitride/hydroxide to accelerate kinetics for oxygen evolution at large current density, *Nat. Commun.* 14 (2023) 1873, <https://doi.org/10.1038/s41467-023-37091-x>.
- [25] T.Y. Xia, L. Zhou, S.Q. Gu, H. Gao, X.Y. Ren, S.F. Li, R.M. Wang, H.Z. Guo, A subtle functional design of hollow CoP/MoS_2 hetero-nanoframes with excellent hydrogen evolution performance, *Mater. Design* 211 (2021), 110165, <https://doi.org/10.1016/j.matdes.2021.110165>.
- [26] P.L. Zhai, Y.X. Zhang, Y.Z. Wu, J.F. Gao, B. Zhang, S.Y. Cao, Y.T. Zhang, Z.W. Li, L. C. Sun, J.G. Hou, Engineering active sites on hierarchical transition bimetal oxides/sulfides heterostructure array enabling robust overall water splitting, *Nat. Commun.* 11 (2020) 5462, <https://doi.org/10.1038/s41467-020-19214-w>.
- [27] Y. Zhao, S.Z. Wei, F.H. Wang, L.J. Xu, Y. Liu, J.P. Lin, K.M. Pan, H. Pang, Hatted 1/2H-Phase MoS_2 on Ni_3S_2 Nanorods for Efficient Overall Water Splitting in Alkaline Media, *Chem-Eur J* 26 (2020) 2034–2040, <https://doi.org/10.1002/chem.201904307>.
- [28] J.W. Zhu, S.C. Mu, Parsing the basic principles to build efficient heterostructures toward electrocatalysis, *Inorg. Chem. Front.* 10 (2023) 2220–2225, <https://doi.org/10.1039/d3qi00117b>.
- [29] H.W. Bai, D. Chen, Q.L. Ma, R. Qin, H.W. Xu, Y.F. Zhao, J.X. Chen, S.C. Mu, Atom Doping Engineering of Transition Metal Phosphides for Hydrogen Evolution Reactions, *Electrochem Energy R* 5 (2022) 24, <https://doi.org/10.1007/s41918-022-00161-7>.
- [30] H.H. Wang, T.T. Ai, W.W. Bao, J.J. Zhang, Y. Wang, L.J. Kou, W.H. Li, Z.F. Deng, J. J. Song, M. Li, Regulating the electronic structure of Ni_3S_2 nanorods by heteroatom vanadium doping for high electrocatalytic performance, *Electrochim. Acta* 395 (2021), 139180, <https://doi.org/10.1016/j.electacta.2021.139180>.
- [31] B. Chong, M.Y. Xia, Y. Lv, H. Li, X.Q. Yan, B. Lin, G.D. Yang, Hierarchical phosphorus-oxygen incorporated cobalt sulfide hollow micro/ nano-reactor for highly-efficient electrocatalytic overall water splitting, *Chem. Eng. J.* 465 (2023), 142853, <https://doi.org/10.1016/j.cej.2023.142853>.
- [32] S.S. Huang, Z.Q. Jin, P. Ning, C.Y. Gao, Y. Wu, X. Liu, P.J. Xin, Z.X. Chen, Y. Jiang, Z.J. Hu, Z.W. Chen, Synergistically modulating electronic structure of NiS_2 hierarchical architectures by phosphorus doping and sulfur-vacancies defect engineering enables efficient electrocatalytic water splitting, *Chem. Eng. J.* 420 (2021), 127630, <https://doi.org/10.1016/j.cej.2020.127630>.
- [33] S.S. Huang, Q. Zhang, P.J. Xin, J. Zhang, Q.C. Chen, J. Fu, Z.Q. Jin, Q. Wang, Z. J. Hu, Construction of Fe-doped NiS-NiS_2 Heterostructured Microspheres Via Etching Prussian Blue Analogues for Efficient Water-Urea Splitting, *Small* 18 (2022) 2106841, <https://doi.org/10.1002/sml.202106841>.
- [34] J.K. Norskov, T. Bligaard, A. Logadottir, J.R. Kitchin, J.G. Chen, S. Pandalov, J. K. Norskov, Trends in the exchange current for hydrogen evolution, *J. Electrochem. Soc.* 152 (2005) J23–J26, <https://doi.org/10.1149/1.1856988>.
- [35] H. Liu, F.X. Ma, C.Y. Xu, L. Yang, Y. Du, P.P. Wang, S. Yang, L. Zhen, Sulfurizing-Induced Hollowing of Co_9S_8 Microplates with Nanosheet Units for Highly Efficient Water Oxidation, *ACS Appl. Mater. Interfaces* 9 (2017) 11634–11641, <https://doi.org/10.1021/acsami.7b00899>.
- [36] H.T. Lei, M.X. Chen, Z.Z. Liang, C.Y. Liu, W.B. Zhang, R. Cao, Ni_2P hollow microspheres for electrocatalytic oxygen evolution and reduction reactions, *Catalysis, Sci. Technol.* 8 (2018) 2289–2293, <https://doi.org/10.1039/C8CY00211H>.
- [37] S.S. Tang, X. Wang, Y.Q. Zhang, M. Courte, H.J. Fan, D. Fichou, Combining Co_3S_4 and $\text{Ni-Co}_3\text{S}_4$ nanowires as efficient catalysts for overall water splitting: an experimental and theoretical study, *Nanoscale* 11 (2019) 2202–2210, <https://doi.org/10.1039/c8nr07787h>.
- [38] G.Q. Gan, X.Y. Li, L. Wang, S.Y. Fan, J. Li, F. Liang, A.C. Chen, Identification of Catalytic Active Sites in Nitrogen-Doped Carbon for Electrocatalytic Dechlorination of 1,2-Dichloroethane, *ACS Catal.* 9 (2019) 10931–10939, <https://doi.org/10.1021/acscatal.9b02853>.
- [39] J. Yin, Q.H. Fan, Y.X. Li, F.Y. Cheng, P.P. Zhou, P.X. Xi, S.H. Sun, Ni–C–N Nanosheets as Catalyst for Hydrogen Evolution Reaction, *J. Am. Chem. Soc.* 138 (2016) 14546–14549, <https://doi.org/10.1021/jacs.6b09351>.
- [40] W.D. Zhang, Q.T. Hu, L.L. Wang, J. Gao, H.Y. Zhu, X.D. Yan, Z.G. Gu, In-situ generated Ni-MOF/LDH heterostructures with abundant phase interfaces for enhanced oxygen evolution reaction, *Appl. Catal. B-Environ* 286 (2021), 119906, <https://doi.org/10.1016/j.apcatb.2021.119906>.
- [41] L.Y. Hu, X. Zeng, X.Q. Wei, H.J. Wang, Y. Wu, W.L. Gu, L. Shi, C.Z. Zhu, Interface engineering for enhancing electrocatalytic oxygen evolution of NiFe LDH/ NiTe heterostructures, *Appl. Catal. B-Environ* 273 (2020), 119014, <https://doi.org/10.1016/j.apcatb.2020.119014>.
- [42] B. He, Q.C. Zhang, Z.H. Pan, L. Li, C.W. Li, Y. Ling, Z.X. Wang, M.X. Chen, Z. Wang, Y.G. Yao, Q.W. Li, L.C. Sun, J. Wang, L. Wei, Freestanding Metal-Organic Frameworks and Their Derivatives: An Emerging Platform for Electrochemical Energy Storage and Conversion, *Chem. Rev.* 122 (2022) 10573–10574, <https://doi.org/10.1021/acs.chemrev.1c00978>.
- [43] S. Cao, H.J. Huang, K. Shi, L. Wei, N. You, X.M. Fan, Z.H. Yang, W.X. Zhang, Engineering superhydrophilic/superaerophobic hierarchical structures of Co-CH@NiFe-LDH/NF to boost the oxygen evolution reaction, *Chem. Eng. J.* 422 (2021), 130123, <https://doi.org/10.1016/j.cej.2021.130123>.
- [44] Z.C. Wang, H.L. Liu, R.X. Ge, X. Ren, J. Ren, D.J. Yang, L.X. Zhang, X.P. Sun, Phosphorus-Doped Co_3O_4 Nanowire Array: A Highly Efficient Bifunctional Electrocatalyst for Overall Water Splitting, *ACS Catal.* 8 (2018) 2236–2241, <https://doi.org/10.1021/acscatal.7b03594>.
- [45] Y.R. Li, Q.F. Guo, Y.M. Jiang, W. Shen, M. Li, R.X. He, A novel ball-in-ball hollow oxygen-incorporating cobalt sulfide spheres as high-efficient electrocatalyst for oxygen evolution reaction, *Chin. Chem. Lett.* 32 (2021) 755–760, <https://doi.org/10.1016/j.ccl.2020.05.012>.
- [46] J.Y. Zhang, W. Xiao, P.X. Xi, S.B. Xi, Y.H. Du, D.Q. Gao, J. Ding, Activating and Optimizing Activity of CoS_2 for Hydrogen Evolution Reaction through the Synergic Effect of N Dopants and S Vacancies, *ACS Energy Lett.* 2 (2017) 1022–1028, <https://doi.org/10.1021/acsenenergylett.7b00270>.
- [47] R.Z. ElSchen, Z.Y. Zhang, Z.C. Wang, W. Wu, S.W. Du, W.B. Zhu, H.F. Lv, N. C. Cheng, Constructing Air-Stable and Reconstruction-Inhibited Transition Metal Sulfide Catalysts via Tailoring Electron-Deficient Distribution for Water Oxidation, *ACS Catal.* 12 (2022) 13234–13246, <https://doi.org/10.1021/acscatal.2c03338>.
- [48] H. Su, S.J. Song, S.S. Li, Y.Q. Gao, L. Ge, W.Y. Song, T.Y. Ma, J. Liu, High-valent bimetal $\text{Ni}_3\text{S}_2/\text{Co}_3\text{S}_4$ induced by Cu doping for bifunctional electrocatalytic water splitting, *Appl. Catal. B-Environ* 293 (2021), 120225, <https://doi.org/10.1016/j.apcatb.2021.120225>.
- [49] Y. Yang, Y.K. Kang, H.H. Zhao, X.P. Dai, M.L. Cui, X.B. Luan, X. Zhang, F. Nie, Z. T. Ren, W.Y. Song, An Interfacial Electron Transfer on Tetrahedral $\text{NiS}_2/\text{NiSe}_2$ Heterocages with Dual-Phase Synergy for Efficiently Triggering the Oxygen Evolution Reaction, *Small* 16 (2019) 1905083, <https://doi.org/10.1002/sml.201905083>.